INTERNATIONAL JOURNAL FOR NUMERICAL METHODS IN FLUIDS
Int. J. Numer. Meth. Fluids 2000; **34**: 479–494

A multigrid finite difference approach to steady flow between eccentric rotating cylinders

Mo-Hong Chou*,[1]

Institute of Mathematics, Academia Sinica, Nankang, Taipei, Taiwan, Republic of China

SUMMARY

A simple finite difference scheme over a non-uniform grid is proposed to solve the two-dimensional, steady Navier–Stokes equations. Instead of the Newton method, a more straightforward line search algorithm is used to solve the resultant system of non-linear equations. By adopting the multigrid methodology, a fast convergence is achieved, at least for low-Reynolds number flow. This scheme is applied, in particular, to flow between eccentric rotating cylinders. The computed results are shown in good agreement with some analytic findings. Copyright © 2000 John Wiley & Sons, Ltd.

KEY WORDS: eccentricity; finite difference; multigrid; non-uniform grid; rotating cylinder

1. INTRODUCTION

Flow between two rotating cylinders is representative of circular Couette flow and serves as a typical configuration in connection with journal bearing problems. For a two-dimensional setting, one is often interested in steady flow subject to various combinations of the cylinders' eccentricity and rotation. For strongly viscous cases, like Stokes flow and its small linear perturbation, some analytic results have been obtained by Wannier [1], DiPrima and Stuart [2], and Ballal and Rivlin [3], among others.

As the Reynolds number is increased from zero, a numerical approach becomes inevitable for coping with the non-linearity. Sood and Elrod [4] have used a finite difference scheme to integrate the time-dependent Navier–Stokes equations until a pseudo-steady state is reached. We are, however, interested in numerical procedures directly related to the steady governing equations. There have been several investigations along this line, such as San Andres and Szeri [5] and Kim [6]. Adoption of this approach will lead to solving a system of coupled non-linear equations, together with its linearized version if the Newton method is used. Obviously, this is not an easy task. In order to control the size of the resultant system, a high-order

* Correspondence to: Institute of Mathematics, Academia Sinica, Nankang, Taipei, Taiwan 11529, Republic of China.
[1] E-mail: chou@math.sinica.edu.tw

Received June 1999
Revised December 1999

approximation method, such as the B-spline Galerkin method, was favored by previous researchers, even though it entailed some mathematical complexity.

In this work we shall show that, at least for low-Reynolds number flow, a simple finite difference scheme can be devised to yield a fast convergence by adopting the multigrid methodology. The simplicity includes replacing the conventional Newton iteration by a more straightforward line search algorithm in which we do not need to compute the Jacobian matrix and solve the related linear problem.

The flow problem is formulated in Section 2 and the numerical method is proposed in Section 3. It is found that the cylinders' mode of rotation closely affects the flow pattern. Several representative cases are discussed in Section 4. A comparison with a first-order perturbation analysis [3] is included for checking of the initial effect of inertia.

2. PROBLEM FORMULATION

Consider a two-dimensional incompressible flow between two cylinders of which at least one has a constant rotation about its axis. The inner cylinder has radius d_1 and center (0, 0), while the outer one has radius $d_2 > d_1$, and center $(\lambda, 0)$, $0 \le \lambda < d_2 - d_1$. This configuration yields an eccentricity $\epsilon = \lambda/(d_2 - d_1)$. The constant angular velocities are denoted by Ω_1 and Ω_2 respectively. The signs of these values indicate their respective senses of rotation (e.g., positive = clockwise). The flow is assumed to be governed by the steady Navier–Stokes equations, which, after non-dimensionalization, are written in terms of vorticity (ω) and the streamfunction (ψ) as follows:

$$\psi_y \omega_x - \psi_x \omega_y = \frac{1}{Re}(\omega_{xx} + \omega_{yy}) \tag{1}$$

$$\psi_{xx} + \psi_{yy} = -\omega \tag{2}$$

$$\psi = 0 \quad \text{and} \quad \nabla\psi \cdot \vec{n} = d_1\Omega_1 \quad \text{on inner cylinder} \tag{3}$$

$$\psi = \psi^* \quad \text{and} \quad \nabla\psi \cdot \vec{n} = -d_2\Omega_2 \quad \text{on outer cylinder} \tag{4}$$

In Equations (1)–(4) the unit normal vector $\vec{n}$ points to the flow field, and ψ^* is a constant but not known *a priori*. The Reynolds number Re is defined as $Re = d_1^2|\bar{\Omega}|/\nu$, where ν = kinematic viscosity and $\bar{\Omega} = \Omega_1$ unless $\Omega_1 = 0$, in which case $\bar{\Omega} = \Omega_2$.

Let $z = x + \mathrm{i}y$. The conformal mapping in terms of the complex variable

$$\zeta = \frac{z + c}{1 + cz}, \quad \text{where } c = \frac{\beta}{1 + \sqrt{1 - \beta^2}} \quad \text{and} \quad \beta = \frac{2\lambda d_1}{d_2^2 - d_1^2 - \lambda^2} \tag{5}$$

transforms the cylinders into a concentric configuration in the ζ-plane. Let $\zeta = \exp(\eta - \mathrm{i}\xi)$. Equations (1)–(4) are accordingly converted into the following:

$$\psi_\eta \omega_\xi - \psi_\xi \omega_\eta = \frac{1}{Re}(\omega_{\xi\xi} + \omega_{\eta\eta}) \tag{6}$$

$$\psi_{\xi\xi} + \psi_{\eta\eta} = -J\omega, \quad \text{where } J = \exp(2\eta)|z'(\zeta)|^2 \tag{7}$$

$$\psi = 0 \quad \text{and} \quad \psi_\eta = \sqrt{J} d_1 \Omega_1 \quad \text{at } \eta = 0 = \text{inner cylinder} \tag{8}$$

$$\psi = \psi^* \quad \text{and} \quad \psi_\eta = \sqrt{J} d_2 \Omega_2 \quad \text{at } \eta = \eta^* = \text{outer cylinder} \tag{9}$$

The unknown constant ψ^* in Equations (4) and (9) is to be determined by the univalence of pressure (p) around the cylinders denoted below by Γ_1 and Γ_2. This condition is derived from the Navier–Stokes equations and reads as

$$0 = Re \oint_\Gamma \mathrm{d}p = \oint_\Gamma \nabla\omega \cdot \vec{n}\, \mathrm{d}s, \quad \text{where } \Gamma = \Gamma_1 \text{ or } \Gamma_2 \tag{10}$$

In theory, the last closed integrals in Equation (10) are the same for Γ_1 and Γ_2 using Green's identity. In practice, their computed values are slightly different. Therefore, ψ^* is indeed determined by satisfying

$$\oint_{\Gamma_1} \nabla\omega \cdot \vec{n}\, \mathrm{d}s + \oint_{\Gamma_2} \nabla\omega \cdot \vec{n}\, \mathrm{d}s = 0 \tag{11}$$

or, in terms of ξ, η co-ordinates

$$P \equiv \int_0^{2\pi} \omega_\eta(\xi, 0)\, \mathrm{d}\xi + \int_0^{2\pi} \omega_\eta(\xi, \eta^*)\, \mathrm{d}\xi = 0 \tag{12}$$

To implement this condition, we introduce the following ancillary problem to be solved once and for all:

$$\omega^\circ_{\xi\xi} + \omega^\circ_{\eta\eta} = 0 \quad \text{and} \quad \psi^\circ_{\xi\xi} + \psi^\circ_{\eta\eta} = -J\omega^\circ \tag{13}$$

$$\psi^\circ(\xi, 0) = \psi^\circ_\eta(\xi, 0) = \psi^\circ_\eta(\xi, \eta^*) = 0 \quad \text{and} \quad \psi^\circ(\xi, \eta^*) = 1 \tag{14}$$

Plugging ω° into Equation (12) will yield a value of $P^\circ \neq 0$. Hence, a solution to Equations (6)–(9) with $\psi^* = 0$ is tried first. The computed P in Equation (12) then offers a correction: $\psi^* = -P/P^\circ$.

3. THE NUMERICAL METHOD

The proposed finite difference scheme starts with generating a proper grid in the ξ, η-plane. If the cylinders are concentric, one can exploit the usual polar grid. To increase the radial

resolution adjacent to the cylinders, a non-uniform radial spacing, such as that controlled by the Legendre abscissa, is economical. However, such a grid is distorted by eccentricity through the conformal mapping (5). Namely, the grid is clustered towards the narrow side of the clearance between the cylinders. A regridding is therefore performed in such a way that the angular spacing around the inner cylinder is uniform. As a consequence, the grid in the computational ξ, η domain is non-uniform in both co-ordinates. One may seek a further mapping to make it uniform in another computational domain in order to facilitate the discretization of derivatives. However, we do not need it here.

Based on such a non-uniform grid, a discretization of the second derivative, such as $\psi_{\xi\xi}$, is given as follows. Let $\{\xi_i | \ -2 \le i \le 2\}$ be the local grid around ξ_0 with spacing $\delta_i = \xi_{i+1} - \xi_i$. We construct the cubic, Lagrange polynomial $\bar{\psi}$, which interpolates ψ over $\{\xi_i | \ -1 \le i \le 2\}$ if $\delta_{-1} \le \delta_0$, while over $\{\xi_i | \ -2 \le i \le 1\}$ if $\delta_{-1} > \delta_0$. Then, the value of $\psi_{\xi\xi}$ is approximated by $\bar{\psi}_{\xi\xi}$ at ξ_0. As shown in Appendix A, such a four-point scheme is of second-order accuracy and reduces to the standard three-point, centered difference scheme if $\delta_{-1} = \delta_0$. For the first derivative, such as ψ_ξ, the above switching can be skipped in that the usual quadratic interpolation is still second-order accurate.

After discretization in this way, the Poisson equations (7) and (13), with Dirichlet boundary conditions, are iteratively solved by the quasi-minimal residual method [7] using incomplete LU-factorization as preconditioner. However, the convergence rate is not good enough. We adopt a multigrid technique to speed it up, as described below.

According to the multigrid practice [8], the original problem is downsized through grid coarsening. In general, some flow properties present rapid change in the normal direction near the physical boundary. Hence, semi-coarsening is preferable to double coarsening for preserving the radial resolution. From the computational point of view, these two strategies can be mixed. For instance, the grid indices $\{i | \ 0 \le i \le 8\}$, with $i = 0$ denoting the boundary, can be downsampled as {0, 1, 2, 4, 6, 8} and {0, 1, 2, 4, 8} for a three-grid scheme. In other words, the grid is gradually coarsened when it is apart from the boundary. The data transfer, i.e., restriction and prolongation, can be quite standard. However, we also seek a possible improvement as follows. Suppose we have a local, five-point grid, X, and the associated data, G, which are either partially unknown or partially to be modified. For data restriction we have $X = \{\xi_{i/2} | \ -2 \le i \le 2\}$ and $G = \{g_{i/2} | \ -2 \le i \le 2\}$, where $\xi_{\pm 1/2}$ are two slave points satisfying the relations $\xi_{-1/2} = (\xi_{-1} + \xi_0)/2$, $\xi_{1/2} = (\xi_0 + \xi_1)/2$, $g_{-1/2} = (g_{-1} + g_0)/2$, and $g_{1/2} = (g_0 + g_1)/2$. After this, $\{g_{-1}, g_0, g_1\}$ are reevaluated so that the new collection $\{g_{i/2} | \ -2 \le i \le 2\}$ can be fitted over X by a cubic polynomial. If this is done over the whole grid, only those g_i values indexed with even integers, except suitable modification next the cylinders, are retained to reflect the grid coarsening. For prolongation we have $X = \{\xi_i | \ -2 \le i \le 2\}$ and $G = \{g_i | \ -2 \le i \le 2\}$, where $\{g_{-1}, g_1\}$ denote the coarse-grid data. Again, the unknown fine-grid data, $\{g_{-2}, g_0, g_2\}$, are determined so that $\{g_i | \ -2 \le i \le 2\}$ can be fitted over X by a cubic polynomial. Details are presented in Appendix A.

In view of these procedures, both restriction and prolongation are performed in an implicit manner, which involves solving a tridiagonal system of linear equations. Such a scheme provides an autoregression for the conventional, area-weighted interpolation, and yields a better performance for the multigrid cycling in terms of iteration count. However, this gain is partly offset by the extra CPU time associated with the implicitness. Further discussions are

presented in Section 4. We note in passing that the cycling is of sawtooth-type because the data are restricted all the way down to the coarsest grid without intermediate relaxation.

An immediate application of this multigrid Dirichlet problem solver is to construct a Stokes corrector, S, to handle the no-slip, or Neumann, boundary conditions present in Equations (8), (9), and (14). Let $0 \le \xi_i \le 2\pi$, $1 \le i \le M+1$, denote the grid's ξ co-ordinates. For $1 \le i \le M$, find two pairs of functions $\{\omega_1, \psi_1\}$ and $\{\omega_2, \psi_2\}$, which are 2π periodic in the ξ variable, and respectively satisfy

$$\Delta\omega_1 = 0, \qquad \Delta\psi_1 = -J\omega_1, \qquad \omega_1(\xi, 0) = \delta(\xi - \xi_i),$$

$$\omega_1(\xi, \eta^*) = \psi_1(\xi, 0) = \psi_1(\xi, \eta^*) = 0 \tag{15}$$

and

$$\Delta\omega_2 = 0, \qquad \Delta\psi_2 = -J\omega_2, \qquad \omega_2(\xi, \eta^*) = \delta(\xi - \xi_i),$$

$$\omega_2(\xi, 0) = \psi_2(\xi, 0) = \psi_2(\xi, \eta^*) = 0 \tag{16}$$

where $\Delta = \partial^2/\partial\xi^2 + \partial^2/\partial\eta^2$ and $\delta(\cdot)$ are Dirac's delta functions. The corrector S is a $2M \times 2M$ matrix whose ith and $(M+i)$th column vectors are formed by $\{\psi_{1,\eta}(\cdot, 0),\ \psi_{1,\eta}(\cdot, \eta^*)\}$ and $\{\psi_{2,\eta}(\cdot, 0),\ \psi_{2,\eta}(\cdot, \eta^*)\}$ respectively. In our experience (see Section 4) each of these columns only took a few multigrid cycles to solve Equations (15) or (16).

Now, we are prepared to state the algorithm for solving the Navier–Stokes equations (6)–(9). Instead of ψ and ω, we regard the convection head, $Q = Re(\psi_\eta\omega_\xi - \psi_\xi\omega_\eta)$, as the unknown. The associated non-linear operator, F, on Q is described by

Algorithm A

1. Given an input of Q, solve the homogeneous Dirichlet problem

$$\Delta\omega = Q, \qquad \Delta\psi = -J\omega,$$

$$\omega(\xi, 0) = \omega(\xi, \eta^*) = \psi(\xi, 0) = \psi(\xi, \eta^*) = 0$$

2. Compute the vector q containing the values $\psi_\eta(\xi_i, 0)$ and $\psi_\eta(\xi_i, \eta^*)$.
3. Use the corrector matrix, S, around Equations (15) and (16) to find the wall–vorticity vector, $\hat{\omega}$, such that $S \cdot \hat{\omega} + q$ equals the ψ_η component in Equations (8) and (9).
4. Solve $\Delta\bar{\omega} = 0$ with $\hat{\omega}$ as the Dirichlet boundary condition, and $\Delta\bar{\psi} = -J\bar{\omega}$ with $\bar{\psi}(\xi, 0) = \bar{\psi}(\xi, \eta^*) = 0$.
5. Set $\omega = \omega + \bar{\omega}$, $\psi = \psi + \bar{\psi}$, and compute the value P in Equation (12).
   (a) If this is the first run, repeat the foregoing steps with Equations (13) and (14) instead of Equations (8), (9), and (17); otherwise, skip this sub-step.
   (b) By virtue of Equations (13) and (14), update the unknown constant ψ^* in Equation (9) by $\psi^* = -P/P^\circ$, and reset $\omega = \omega + \psi^*\omega^\circ$, $\psi = \psi + \psi^*\psi^\circ$.
6. $F(Q) = Re(\psi_\eta\omega_\xi - \psi_\xi\omega_\eta)$.

Note that for Stokes flow, the algorithm reduces to steps 3–5, in that we have $Q = 0$, and steps 1, 2, and 6 are either trivial or not needed. If $Re > 0$, our goal is to find a Q such that $F(Q) = Q$. This is a system of non-linear equations, and is usually tackled by the Newton method. However, constructing the associated Jacobian matrix and solving the related linear problem is clearly not an easy task. As an alternative, Algorithm A is augmented with the following line search method, and is called Algorithm B. Namely

Algorithm B

1. Given an initial guess, Q, find $Q^* = F(Q)$ by Algorithm A.
2. Solve the one-dimensional minimization problem

$$\min f(\mu) \quad \text{for } \mu \in [0, 1]$$

$$\text{where } f(\mu) = \|F(Q + \mu(Q^* - Q)) - (Q + \mu(Q^* - Q))\|^2 \tag{18}$$

   In Equation (18), $\|\cdot\|$ denotes the Euclidian norm, and, in fact, $f(\mu)$ is a quartic polynomial. So the minimization can be done without much ado.
3. Denote the minimizer of Step 2 by μ^*, and reset $Q = Q + \mu^*(Q^* - Q)$.
4. Go back to Step 1 and repeat the whole process until $\|Q^* - Q\|/\|Q\|$ is smaller than some prescribed tolerance.

Although it is a descent scheme, Algorithm B performs well only for flow with small Reynolds number. As a cure again, we use the multigrid methodology, whose ingredients, such as grid coarsening and data restriction and prolongation, are much the same as those discussed above for the Poisson equation (also see Appendix A). Since we are dealing with a non-linear problem, the so-called full approximation scheme (FAS) [8] is adopted for coarse-grid relaxation. Moreover, the sawtooth cycling for the linear problem is replaced here by the more standard V- or even W-cycling for increased Reynolds number.

When Algorithm B is finished, ψ and ω come out as byproducts. If the pressure field, p, is wanted, it can be obtained from the modified Bernoulli head, $\mathscr{B} = Re(p + (\psi_\xi^2 + \psi_\eta^2)/2J)$, by solving the problem

$$\mathscr{B}_{\xi\xi} + \mathscr{B}_{\eta\eta} = Re(J\omega^2 - \psi_\xi \omega_\xi - \psi_\eta \omega_\eta) \tag{19}$$

$$\mathscr{B}(\xi, 0) = -\int_0^\xi \omega_\eta \, \mathrm{d}\xi \quad \text{and} \quad \mathscr{B}_\eta(\xi, \eta^*) = \omega_\xi - Re\, \omega\psi_\eta \tag{20}$$

4. WORKED EXAMPLES AND DISCUSSIONS

The flow is examined under the settings summarized in Table I. The reader is referred to Section 2 for the notations. The computational ξ, η domain is covered by an 80×24,

Table I. Flow configurations.

Case	d_1	d_2	λ	Ω_1	Ω_2
1	1	2	0.5	−1	0
2	1	2	0.5	0	−1
3	1	2	0.5	1	−0.5
4	1	2	0.7	−1	−0.5

non-uniform grid, whose resolution might not be fine enough but satisfies the expository purpose. All the computations were run on an Intel-based PC.

We begin with computing the Stokes flow, for which the result can be verified by some analytic findings [1,3]. In this work, Wannier's formula [1] is employed to check on the numerical accuracy, and the comparisons are summarized in Table II. Note that, for pressure field, only $Re p$ is meaningful, as p becomes unbounded as Re tends to zero.

The multigrid performance of our scheme is further examined against the more standard approach. To distinguish these approaches we use the index system: (i, j, k), where i denotes the order of discretization (i.e., 1 = standard three-point scheme; 2 = our four-point scheme); j denotes the manner of prolongation and restriction (i.e., 1 = standard three-point, explicit scheme; 2 = our three-point, implicit scheme); k denotes the manner of grid coarsening (i.e., 1 = standard semi-coarsening; 2 = our near double-coarsening). Since the employed grid is non-uniform in both ξ- and η-directions, we introduce for each multigrid level an approximated mesh size: $h \approx (m \times n)^{-1/2}$, where m and n are the respective grid numbers in each direction.

The log–log plots of Figure 1 show a definite order of convergence associated with grid refinement. For cases 112 and 122, this order is 2.1 for the streamfunction and 2.4 for the vorticity; while for cases 212 and 222 we have 2.6 for streamfunction and 1.8 for vorticity. Although the standard three-point discretization presents a superconvergence (i.e., one order higher than its formal estimate associated with a non-uniform grid), our four-point discretization still performs better in that the overall relative error is reduced by a factor of 3 at the expense of 10% increase in CPU time, as shown in Figure 1.

The effect of autoregression in multigrid data transfer is shown in Figure 2, where we plot the finest grid's convergence history associated with constructing the Stokes corrector discussed in Section 3. In view of cases 112 and 122, autoregression does reduce the iteration

Table II. Root-mean-square error, $\|\text{numeric} - \text{analytic}\|/\|\text{analytic}\|$, for Stokes flow.

	Case 1	Case 2	Case 3	Case 4
ψ	9.6E−5	3.3E−4	2.8E−4	5.9E−4
ω	6.4E−4	1.2E−3	4.9E−4	1.4E−3
$Re p$	1.0E−3	1.3E−3	1.9E−3	1.8E−3

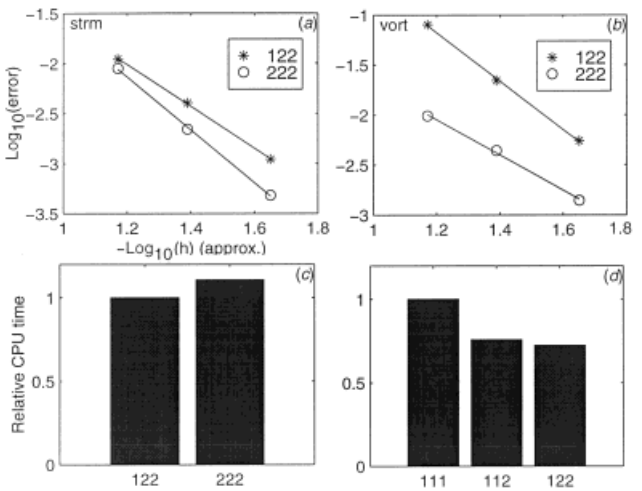

Figure 1. (a) and (b) Convergence behavior against grid refinement for three-point (∗) and four-point (○) discretizations; (c) and (d) relative CPU times for different schemes discussed in the text.

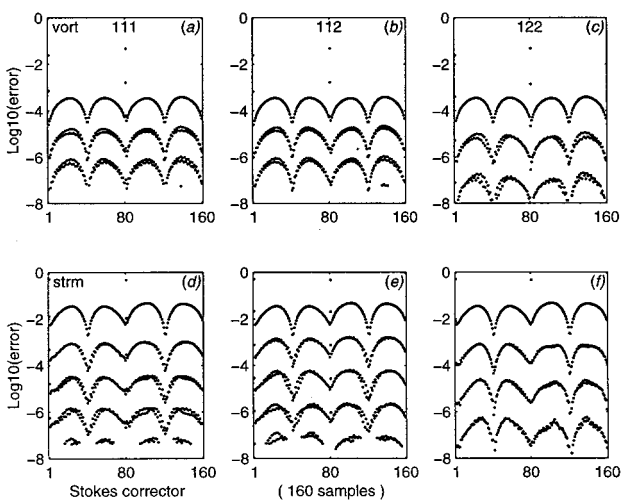

Figure 2. Convergence histories for computing the Stokes corrector by different schemes discussed in the text, where 160 samples of boundary conditions are used. (a)–(c) Vorticity (vort); (d)–(f) streamfunction (strm).

count. However, this gain is partly offset by the associated implicitness, and the CPU time is reduced slightly in the present study.

Also shown in Figure 2 is a comparison between grid semi-coarsening and near double-coarsening. In view of cases 111 and 122, it is adequate to only preserve the radial resolution

near the boundary for catching possible rapid change. By doing so, a significant saving of both iteration count and CPU time can be achieved (also see Figure 1).

Figures 3 and 4 show that the cylinders' mode of rotation closely affects the flow pattern, and the first influence of inertia is the break of flow symmetry with respect to the x-axis. To find the steady state with increasing non-linearity, one may need some continuation process to get a good initial guess. That is, the associated Reynolds number is incrementally increased up to the target value, and each of the intermediate results serves as the initial guess for the next stage. Such a need can be greatly relaxed by multigrid techniques, as introduced in Section 3.

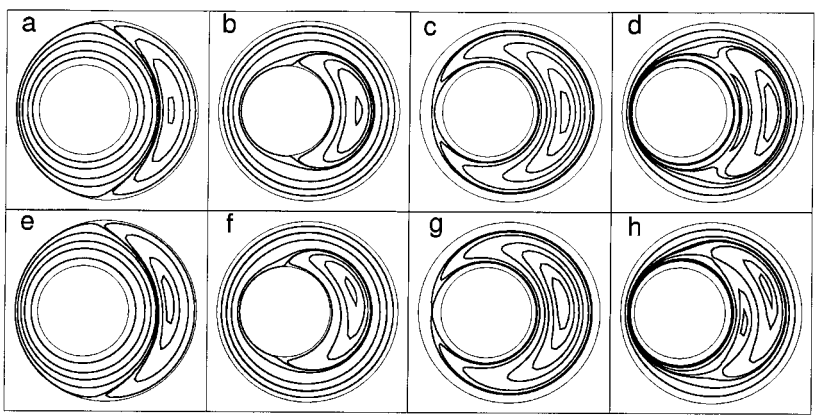

Figure 3. Streamlines for configurations listed in Table I. (a)–(d) Stokes flow; (e)–(h) flow with $Re = 40$; for cases 1–4 respectively.

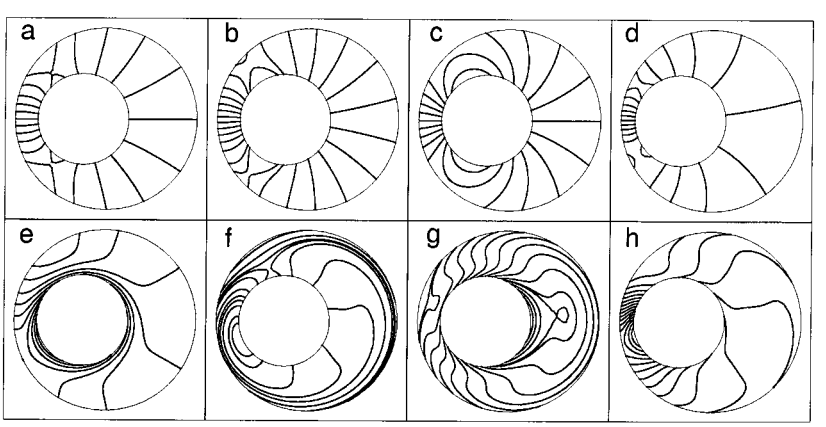

Figure 4. Pressure fields (Rep) for configurations listed in Table I. (a)–(d) Stokes flow; (e)–(h) flow with $Re = 40$; for cases 1–4 respectively.

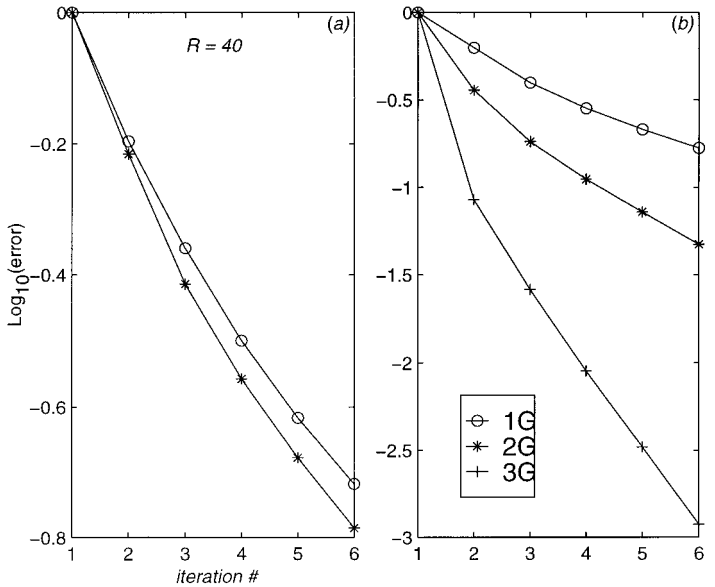

Figure 5. (a) Single-grid computation for flow with $Re = 40$, initiated by flow with $Re = 0$ ($\bigcirc$) and $Re = 30$ ($*$) respectively; (b) multigrid counterpart initiated by flow with $Re = 0$.

A comparison is presented in Figure 5, where we see Stokes flow serve as a good initiation for multigrid viscous flow computations. The convergence histories of a three-grid simulation for flow situations listed in Table I are surveyed in Figure 6, for $Re \leq 40$. Certainly, it also works for larger Re but we have to increase the grid resolution accordingly.

Next, we provide some quantitative results concerning the influence of Reynolds number on certain locations, such as the recirculation eddy's center and closure point. If the latter is located on one of the cylinders, it split into the separation and reattachment points. These locations are measured by the polar angle (θ) with respect to the inner cylinder's center and the positive real axis.

Figure 7 presents the results for cases 1 and 2 in Table I, where either the inner or the outer cylinder is rotating counterclockwise, but the other one is stationary. Clearly, the initial influence of inertia on both the separation and reattachment points is quite small. The computed values of $\partial\theta/\partial Re$ at $Re = 0$ are -5.2×10^{-3} (case 1) and -1.2×10^{-2} (case 2) for separation; -4.5×10^{-3} (case 1) and 4.9×10^{-3} (case 2) for reattachment. They reveal that, initially, both the separation and reattachment points of case 1 move in the direction opposite to the cylinder's rotation, while a parallel direction is found for the reattachment point in case 2. Except the last fact, these results are in good agreement with analytic findings of Ballal and Rivlin [3]. This exception is related to eccentricity, and will be further examined later.

As the Reynolds number increases, we see from Figure 7 the separation point on the stationary cylinder still moves in the direction opposite to the rotating cylinder. The reattachment point, on the other hand, moves in the parallel direction. Quantitatively, these movements are still small for case 1. In either case we see the separation point moves more

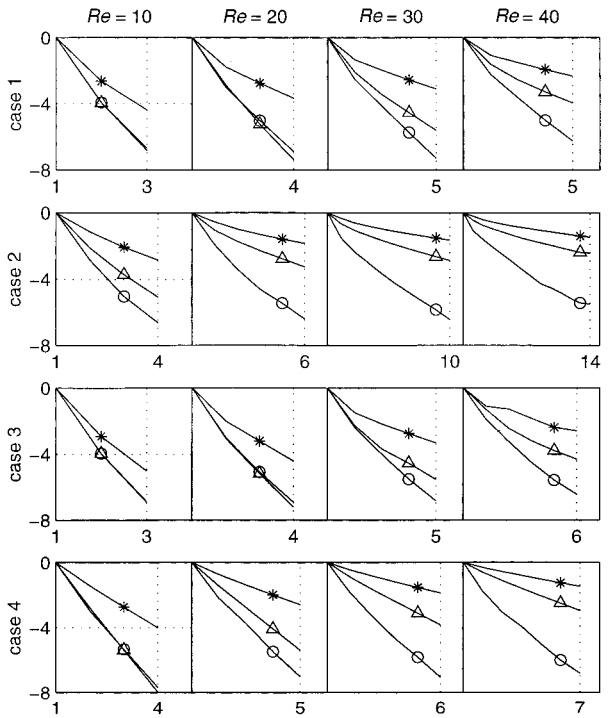

Figure 6. Multigrid convergence histories, $\log_{10}(\|Q_n^* - Q_n\|/\|Q_1^* - Q_1\|)$ against the iteration index n, for configurations listed in Table I, for $Re = 10$, 20, 30, 40; — ∗ —, one-grid; — △ —, two-grid; — ○ —, three-grid.

significantly than the reattachment point, but the difference is not so remarkable as found by San Andres and Szeri [5]. They also predicted a rotation sense opposite to the first-order perturbation [3] and the present work.

When both cylinders are rotating, i.e., cases 3 and 4 in Table I, the recirculation eddy's closure point becomes located in the interior of the flow field. Figure 8 summarizes the evolution of eddy center and interior closure point (if any) for cases 1–4. As shown in Figure 8(a), the eddy center always moves in the direction parallel to the rotating cylinder for cases 1 and 2. This is a common finding in existing literature. In case 3, where the cylinders are counter-rotating, the interior closure point is located in the narrow side of the flow field (see Figure 3). As shown in Figure 8(b), this point is slightly moved with the Reynolds number in the direction parallel to the inner cylinder's rotation, while the eddy center is moved in the direction parallel to the outer cylinder.

Figure 8(c) and (d) show the results of case 4 in which both cylinders are rotating in the same sense. There are two eddies sharing a pair of closure points as shown in Figure 3. In response to the inertial effect, both the eddy near the outer cylinder and the upper closure

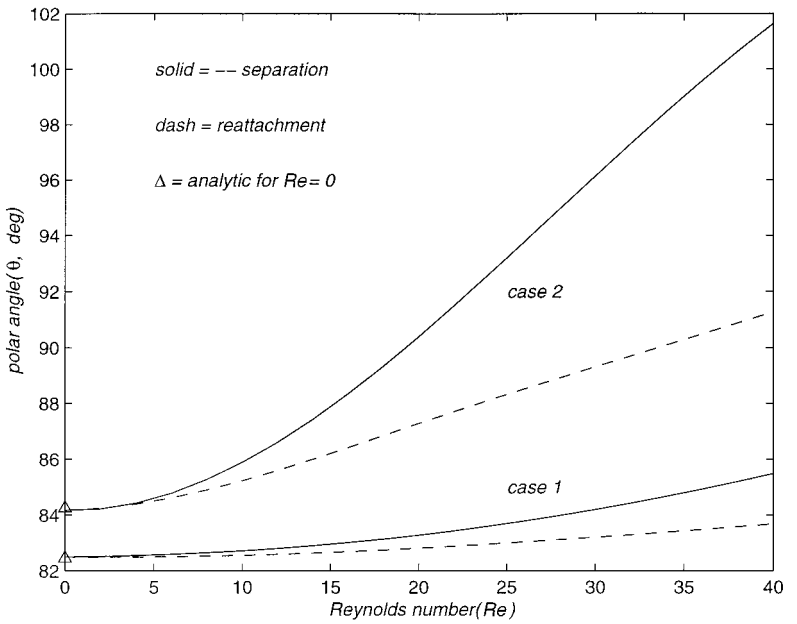

Figure 7. Polar angle (in degree) of separation point (solid, negative) and reattachment point (dash), versus Reynolds number for cases 1 and 2 in Table I. Symbol (△): analytic result for $Re = 0$.

point move in the direction parallel to the cylinders' rotation. However, the eddy near the inner cylinder moves with the Reynolds number in the direction opposite to both cylinders, and in an increase-then-decrease fashion. This is also true for the lower closure point, but it moves in the parallel direction. Similar phenomena were observed by Ballal and Rivlin [3], but they used the ratio of the cylinders' rotating speeds instead of Reynolds number.

Finally, we extend the study of case 2 to cover the variation of eccentricity(ϵ), $0 \leq \epsilon \leq 1$. Figure 9(a)–(c) respectively plots ϵ against the polar angle θ of the separation point, the reattachment point, and the eddy center. In these figures, the Reynolds number serves as a parameter. It is easy to see that the recirculation region increases with eccentricity, while its separation and reattachment points are slowly varied with Reynolds number. For small ϵ, the increase of Reynolds number also makes both the separation point and the eddy center move in the direction opposite to the outer cylinder's rotation. Some clues for this observation are provided by a uniform flow past a rotating cylinder [9,10].

The initial influences of inertia on the locations of these stagnation points, i.e., $\partial\theta/\partial Re$ at $Re = 0$, are shown in Figure 9(d)–(f) respectively. As far as the rotation sense is concerned, we see both the separation and reattachment points are opposite to the outer cylinder for small ϵ. However, they each have a critical value of ϵ beyond which the sense is reversed. That is, $\epsilon \sim 0.45$ for reattachment and $\epsilon \sim 0.6$ for separation. In response to this change, the eddy center reaches a local peak in its movement at $\epsilon \sim 0.5$, although its sense is always parallel to

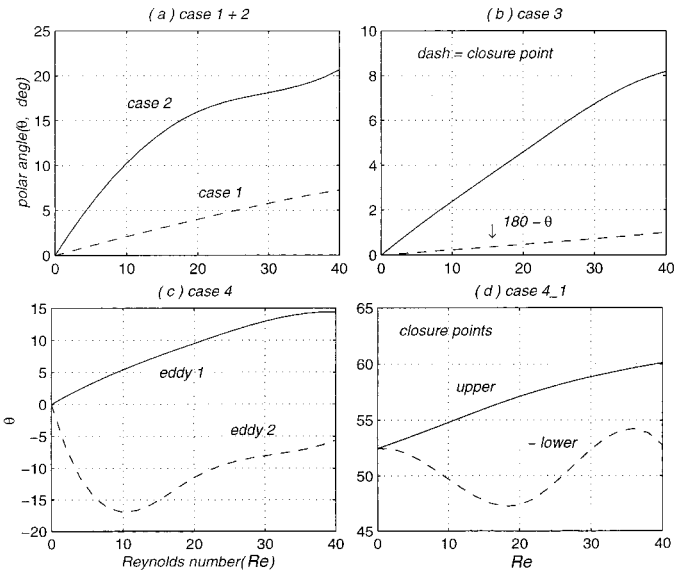

Figure 8. Polar angle (in degree) of eddy center and interior closure point (if any), versus Reynolds number for configurations listed in Table I. (a) Cases 1 and 2; (b) case 3; (c) and (d) case 4.

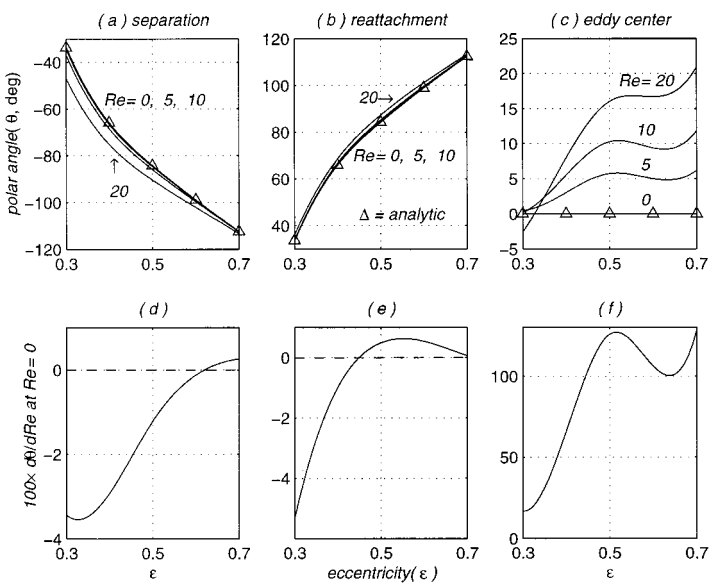

Figure 9. Polar angle (θ in degrees) of (a) separation point, (b) reattachment point, and (c) eddy center, versus eccentricity. $\Omega_1 = 0$, $\Omega_2 = -1$, and $Re = 0,\ 5,\ 10,\ 20$ respectively. Symbol ($\triangle$): analytic result for $Re = 0$. (d)–(f) Partial derivatives, $100 \times \partial\theta/\partial Re$ at $Re = 0$, drawn out of (a)–(c) respectively.

the outer cylinder. The existence of such a critical eccentricity has been demonstrated, with certain discrepancies, by first-order perturbation analysis [3] and the B-spline Galerkin method [5]. Our result is closer to the former.

5. CONCLUSION

A multigrid finite difference scheme is employed to investigate the steady flow between eccentric rotating cylinders. This scheme is both simple and efficient for viscous flow simulation. The influence of Reynolds number as well as the eccentricity on certain flow properties has been examined. Among the demonstrations, the numerical results are shown in good agreement with analytic findings about the initial effect of inertia.

ACKNOWLEDGMENTS

The author is grateful to the referee for valuable comments. This research work was supported in part by the National Science Council under grant NSC87-2119-M-001-001.

APPENDIX A. SOME INTERPOLATION FORMULAS

Let f be a function whose values are given by $\{f_i | \ -2 \le i \le 2\}$ over the discrete mesh $\{-\alpha h, \ -\beta h, 0, h, \gamma h\}$, where $\alpha > \beta > 0$, $\gamma > 1$, and h is a generic mesh size. Fitting f over $[-\beta h, h]$ by a quadratic polynomial gives an approximate second derivative at 0

$$\ddot{f}(0) = \frac{2}{h^2}\left(\frac{f_{-1}}{\beta(1+\beta)} - \frac{f_0}{\beta} + \frac{f_1}{1+\beta}\right) \tag{21}$$

Using Taylor expansion, we have the following error estimate:

$$\ddot{f}(0) \doteq f''(0) - \frac{(\beta-1)h}{3} f^{(3)}(0) + \frac{(1-\beta+\beta^2)h^2}{12} f^{(4)}(0) \tag{22}$$

Hence, the approximation (21) is second-order accurate only if $\beta = 1$.

Now we fit f over $[-\alpha h, h]$ by a cubic polynomial. The approximated $f''(0)$ becomes

$$\ddot{f}^{-}(0) = \frac{2}{h^2}\left(\frac{(1-\beta)f_{-2}}{\alpha(1+\alpha)(\alpha-\beta)} + \frac{(\alpha-1)f_{-1}}{\beta(1+\beta)(\alpha-\beta)} - \frac{(\alpha+\beta-1)f_0}{\alpha\beta} + \frac{(\alpha+\beta)f_1}{(1+\alpha)(1+\beta)}\right) \tag{23}$$

The corresponding Taylor expansion is given by

$$\ddot{f}^{-}(0) \doteq f''(0) + \frac{(\alpha+\beta-\alpha\beta)h^2}{12} f^{(4)}(0) \tag{24}$$

If we fit f over $[-\beta h, \gamma h]$ by a cubic polynomial, the counterpart is

$$\ddot{f}^{+}(0) = \frac{2}{h^2}\left(\frac{(1+\gamma)f_{-1}}{\beta(1+\beta)(\beta+\gamma)} - \frac{(1+\gamma-\beta)f_0}{\beta\gamma} + \frac{(\beta-\gamma)f_1}{(1+\beta)(1-\gamma)} + \frac{(\beta-1)f_2}{\gamma(\gamma-1)(\beta+\gamma)}\right) \tag{25}$$

and

$$\ddot{f}^{+}(0) \doteq f''(0) + \frac{(\beta-\gamma+\beta\gamma)h^2}{12} f^{(4)}(0) \tag{26}$$

In view of Equations (24) and (26), we obtain a class of second-order accurate discretizations for $f''(0)$. Such discretizations reduce to the standard three-point formula when $\beta = 1$. One can try any combination of formulas (23) and (25), but the stencil's sign pattern will become uncertain. To be sure, we use formula (23) if $\beta \geq 1$ and formula (25) otherwise.

The next aim is to smooth f. To this end, simple two-point averages are inserted in between the mesh points, such as

$$\bar{f}_{-1/2} \equiv \bar{f}(-\beta h/2) = (f_{-1} + f_0)/2 \quad \text{and} \quad \bar{f}_{1/2} \equiv \bar{f}(h/2) = (f_0 + f_1)/2 \tag{27}$$

Assuming $\bar{f}$ over $\{-\beta h, -\beta h/2, 0, h/2, h\}$ is depicted by a cubic polynomial yields the following condition:

$$\frac{\bar{f}_{-1}}{(\beta+1)(2\beta+1)} + \bar{f}_0 + \frac{\beta^2 \bar{f}_1}{(\beta+1)(\beta+2)} = \frac{4\bar{f}_{-1/2}}{(\beta+1)(\beta+2)} + \frac{4\beta^2 \bar{f}_{1/2}}{(\beta+1)(2\beta+1)} \tag{28}$$

For a uniform mesh, Fourier analysis of Equation (28) gives the frequency domain's amplification factor $\sigma = 2(1+\cos\theta)/(3+\cos\theta)$ for $0 \leq \theta \leq \pi$. By comparing it with the standard raised cosine, $\sigma = (1+\cos\theta)/2$, a better low-pass filtering is achieved.

In connection with the multigrid, data restriction is done by dropping those odd-indexed $\bar{f}$ values obtained through Equation (28); while data prolongation is performed by replacing the right-hand sides of Equation (27) with coarse grid points and values.

REFERENCES

1. Wannier GH. A contribution to the hydrodynamics of lubrication. *Quarterly of Applied Mathematics* 1950; **8**(1): 1–32.
2. DiPrima RC, Stuart JT. Flow between eccentric rotating cylinders. *ASME Journal of Lubrication Technology* 1972; **94**: 266–274.
3. Ballal BY, Rivlin RS. Flow of Newtonian fluid between eccentric rotating cylinders: inertial effects. *Archive for Rational Mechanics and Analysis* 1976; **62**: 237–294.
4. Sood DR, Elrod Jr. HG. Numerical solution of the incompressible Navier–Stokes equations in doubly-connected regions. *AIAA Journal* 1974; **12**(5): 636–641.
5. San Andres A, Szeri AZ. Flow between eccentric rotating cylinders. *Journal of Applied Mechanics* 1984; **51**: 869–878.
6. Kim E. A mixed Galerkin method for computing the flow between eccentric rotating cylinders. *International Journal for Numerical Methods in Fluids* 1998; **26**: 877–885.

7. Freund RW, Nachtigal NM. QMR: a quasi-minimal residual method for non-Hermitian linear systems. *Numerische Mathematik* 1991; **60**: 315–339.
8. Brandt A. Guide to multigrid development. In *Multigrid Methods*, *Lecture Notes in Mathematics*, vol. 960, Hackbush W, Trottenberg U (eds). Springer-Verlag: Berlin, 1982; 220–312.
9. Badr HM, Coutanceau M, Dennis SCR, Ménard C. Unsteady flow past a rotating circular cylinder at Reynolds numbers 10^3 and 10^4. *Journal of Fluid Mechanics* 1990; **220**: 459–484.
10. Chou MH. Numerical study of vortex shedding from a rotating cylinder immersed in a uniform flow field. *International Journal for Numerical Methods in Fluids* 2000; **32**: 545–567.

